Key Points:
- Bright Jovian main auroral emission coincided with enhanced magnetospheric azimuthal and radial magnetic field and increased plasma pressure
- This represents the first evidence of control of Jupiter's main auroral emission intensity by magnetosphere-ionosphere coupling currents
- Modeling of the magnetosphere-ionosphere coupling and radial force balance currents yields results consistent with observations

An Enhancement of Jupiter's Main Auroral Emission and Magnetospheric Currents

J. D. Nichols[1] [iD], F. Allegrini[2,3] [iD], F. Bagenal[4] [iD], E. J. Bunce[1] [iD], S. W. H. Cowley[1] [iD], R. W. Ebert[2,3] [iD], D. Grodent[5], E. Huscher[4], A. Kamran[1], W. S. Kurth[6] [iD], R. J. Wilson[4] [iD], and Z. Yao[5] [iD]

[1]Department of Physics and Astronomy, University of Leicester, Leicester, UK, [2]Southwest Research Institute, San Antonio, TX, USA, [3]Department of Physics and Astronomy, University of Texas at San Antonio, San Antonio, TX, USA, [4]Laboratory for Atmospheric and Space Physics, University of Colorado Boulder, Boulder, CO, USA, [5]Laboratory for Planetary and Atmospheric Physics, Université de Liège, Institut d'Astrophysique et de Géophysique-B5c, Liége, Belgium, [6]Department of Physics and Astronomy, University of Iowa, Iowa City, IA, USA

Abstract We present observations of Jupiter's magnetic field and plasma obtained with the NASA Juno spacecraft during February 2018, along with simultaneous Hubble Space Telescope (HST) observations of the planet's auroras. We show that a few-day transient enhancement of the azimuthal and radial magnetic fields and plasma temperature was coincident with a significant brightening of Jupiter's dawn-side main auroral emission. This presents the first evidence of control of Jupiter's main auroral emission intensity by magnetosphere-ionosphere coupling currents. We support this association by self-consistent calculation of the magnetosphere-ionosphere coupling and radial force balance currents using an axisymmetric model, which broadly reproduces the Juno magnetic field and plasma observations and the HST auroral observations. We show that the transient enhancement can be explained by increased hot plasma pressure in the magnetosphere together with increased iogenic plasma mass outflow rate. Overall, this work provides important observational and modeling evidence revealing the behavior of Jupiter's giant magnetosphere.

1. Introduction

The dynamics of Jupiter's magnetosphere are dominated by planetary rotation, combined with the centrifugal outflow of plasma originating from the volcanic moon Io (e.g., Vasyliunas, 1983). The effects are particularly evident in the middle magnetosphere, where the magnetic field is radially distended into a magnetodisc configuration (Connerney et al., 1981; Khurana & Schwarzl, 2005; Smith et al., 1974). Iogenic plasma corotates with the the planet at small distances, but in the middle magnetosphere conservation of angular momentum leads to a significant decrease in the angular velocity of the outward diffusing iogenic plasma. With no torques acting on the plasma, its angular velocity would decrease with the square of radial distance. However, this radial gradient in the plasma angular velocity, when mapped along the magnetic field, causes an equatorward current to flow in the Pedersen conducting layer of the ionosphere in both northern and southern hemispheres, the $\mathbf{j} \times \mathbf{B}$ force of which balances ion-neutral drag. This torque is communicated via field-aligned currents to the equatorial magnetosphere where a radially outward directed current, associated with sweepback of the magnetic field lines out of the meridian planes (i.e., giving rise to a nonzero azimuthal magnetic field component), acts to speed the magnetospheric plasma back toward corotation (Hill, 1979). A schematic of this current system and the associated field perturbations is shown in Figure 1. The upward directed component of the field-aligned currents, associated with downward precipitating electrons, has in recent years been held responsible for Jupiter's main auroral emission (ME) (Cowley & Bunce, 2001; Hill, 2001; Southwood & Kivelson, 2001), the most stable and often brightest component of Jupiter's auroras broadly comprising a distorted few-degree wide oval at around ~15° colatitude (Clarke et al., 2009; Grodent et al., 2003). The steady state angular velocity profile is dependent on the Pedersen conductivity, the iogenic plasma mass outflow rate, and the magnetodisc field structure (Cowley et al., 2002; Hill, 1979; Nichols & Cowley, 2003, 2004). The latter is associated with an azimuthal current arising from radial stress balance in the magnetosphere (Caudal, 1986; Mauk & Krimigis, 1987). The $\mathbf{j} \times \mathbf{B}$ force of the azimuthal current balances the typically outward forces of plasma pressure gradient, plasma pressure anisotropy, and the centrifugal force associated with the rotating plasma. Thus, the magnetosphere-ionosphere
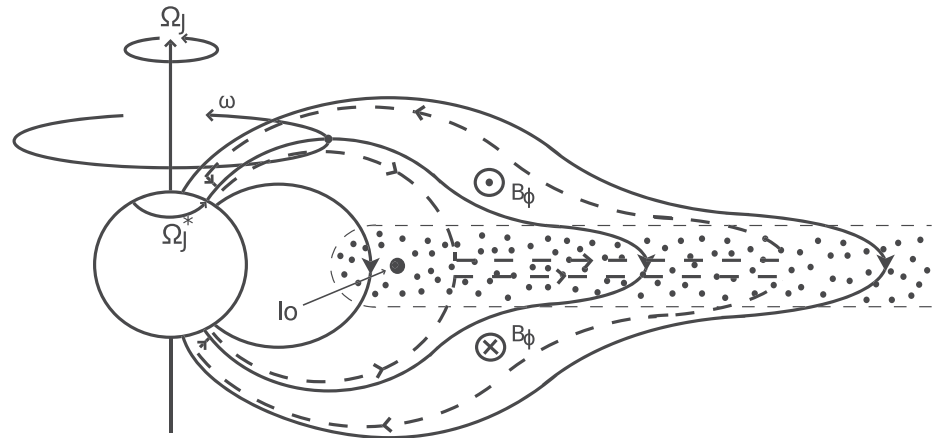
Figure 1. Schematic showing a cut through a meridian plane of Jupiter's inner and middle magnetosphere. The solid lines show the magnetic field lines, while the dashed lines show the magnetosphere-ionosphere coupling currents. The sense of azimuthal field produced by the field-perpendicular currents is indicated as labeled. From Cowley and Bunce (2001).

(M-I) coupling and magnetodisc current systems are strongly coupled and have been self-consistently modeled by Nichols (2011a) and Nichols et al. (2015) based on plasma parameters constrained by Voyager and Galileo observations.

The above description of the origin of Jupiter's main auroral emission, put forward by Cowley and Bunce (2001), Hill (2001), and Southwood and Kivelson (2001), has become the predominant paradigm, and the theory has since been developed in numerous different ways. For example, the effects on the system of the precipitation-modulated Pedersen conductivity, iogenic mass outflow rate, field-aligned voltages, ionospheric composition and flows, diurnal variations, modulation by the solar wind, and magnetodisc structure have all been studied (e.g., Cowley et al., 2002, 2005, 2007; Nichols & Cowley, 2003, 2004, 2005; Ray et al., 2010, 2014; Smith & Aylward, 2009; Tao et al., 2009, 2010). Remarkably, however, prior to the arrival at Jupiter of the NASA spacecraft Juno, there has been no opportunity to test this picture with simultaneous observations of the field and plasma in the middle magnetosphere and the auroral emission. Indeed, there remain unanswered questions, such as why the ME brightens considerably following magnetospheric compression when a simple picture of conservation of angular momentum of rotating plasma indicates that it should dim under such conditions, though we note there are important caveats to this idea concerning the timescale of the response of the ionospheric neutrals to perturbations (Cowley et al., 2007). Initial reports of the first in situ Juno data presented little evidence of field-aligned currents and "inverted-V" structures in electron energy spectra indicative of accelerated field-aligned beams above the auroral zone (Allegrini et al., 2017; Connerney, Adriani, et al., 2017; Mauk et al., 2017; Szalay et al., 2017). More recently, however, evidence of such phenomena has been reported (Clark et al., 2017; Kotsiaros et al., 2019), with the location and strength of the observed magnetic signatures associated with field-aligned currents essentially consistent with the predictions of Cowley et al. (2008, 2017) based on the theory of Cowley and Bunce (2001), though with evidence of localized variation that is perforce not captured by axisymmetric models.

Louarn et al. (2016) demonstrated a correlation between the azimuthal magnetic field and Jovian radio power observed by the Galileo spacecraft. This suggested a link between auroral intensity and azimuthal torque, with variations resulting from changes in the iogenic mass outflow rate between $\sim$150 and 3,000 kg s^{-1}, though they did not establish which auroral component was responding. Kotsiaros et al. (2019) recently demonstrated a spatial association of Juno observations of far ultraviolet (FUV) auroral color ratios with azimuthal field perturbations associated with field-aligned currents. Yao et al. (2019) presented Juno field and plasma observations along with Hubble Space Telescope (HST) observations of Jupiter's auroras obtained in March 2017 and suggested that the observed intensity of Jupiter's main auroral emission was related to variation in the quantity of magnetic flux in the system owing to episodic plasma release down the tail. However, their observations were obtained at radial distances of $\sim$60 $-$80 R_{J}, significantly further than the
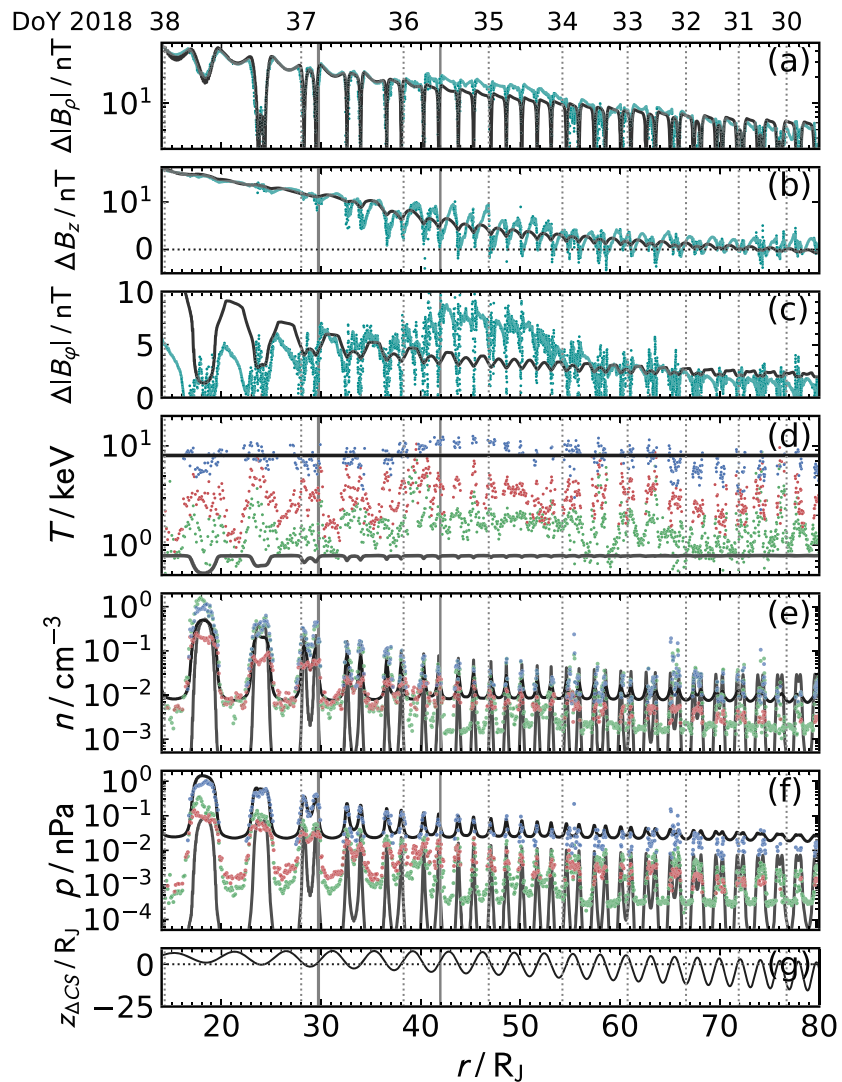
Figure 2. Plot showing the Juno MAG magnetic field and JADE plasma observations obtained during early 2018 versus radial distance in R_J. Panels (a)–(c) show the residual magnetic field components in System III magnetic cylindrical coordinates, ΔB_ρ, ΔB_z, and ΔB_ϕ, respectively, in nT. Juno data are shown in cyan, while model results (discussed in section 3) are shown in black. Panels (d)–(f) show plasma temperature T in keV, number density n in cm^{-3}, and pressure p in nPa, respectively. Blue, red, and green indicate values for heavy ions, protons, and electrons, respectively, while the black and gray lines show model values for the hot and cold plasma, respectively. Panel (g) shows the height in R_J above the Khurana (1992) model current sheet. Vertical dotted lines in all panels are day of year markers, as labeled at the top. The vertical solid gray lines indicate the times of the HST observations, corrected for one-way light travel time.

mapped equatorial distances of the ME of $\sim 20 - 30 \, R_J$, and they did not calculate the auroral currents flowing in the system. Here we present observations of changing intensity of the ME as observed with HST, along with the first simultaneous variations in the M-I coupling and magnetodisc currents and plasma parameters throughout the middle magnetosphere. We show that a transient brightening of the ME was directly associated with increased azimuthal magnetic field (hence torque on the middle magnetospheric plasma), along with enhanced radial field (hence radial forces) and plasma temperatures. This represents the first direct evidence of a connection between varying ME intensity and the M-I coupling currents. We support this association by self-consistent calculation of the M-I coupling currents and the radial force balance currents using an axisymmetric physics-based model, which broadly

reproduces the Juno magnetic field and plasma observations and the HST auroral observations. We show that the transient enhancement can be explained by variation in the hot plasma pressure in the magnetosphere and in the iogenic plasma mass outflow rate.

2. Data

2.1. Juno Data

We employ Juno magnetic field and plasma data from the fluxgate magnetometer (MAG) (Connerney, Benn, et al., 2017) and the Jupiter Auroral Distributions Experiment (JADE) (McComas et al., 2017) as shown in Figure 2. These data were obtained during early 2018 as the spacecraft was inbound prior to peri-jove (PJ) 11. During this interval Juno traversed the outer to middle magnetosphere at around $\sim$3 hr LT, repeatedly crossing the current sheet at the planetary rotation period until the spacecraft was inside $\sim$20 R_J. This interval is of particular interest since between Days 33 and 36, while the spacecraft was at radial distances between $\sim$57 and 36 R_J, the field and plasma were subject to deviations from their usual states, as is discussed below. The top three panels of Figure 2 show with cyan points the residual field components in System III magnetic cylindrical coordinates (ρ, z, ϕ) at 60 s resolution, after subtraction of the internal magnetic field as given by the JRM09 field model (Connerney et al., 2018). The following three panels show numerical plasma moments (specifically, plasma temperature T, pressure p, and number density n) for the heavy ions (blue), protons (red), and electrons (green). The JADE instrument measures ions from $\sim$5 eV to $\sim$50 keV and electrons from $\sim$0.1 to 100 keV. The JADE-I ion data have been calculated using the in-flight calibration parameters described in Kim et al. (2019). The JADE-E electron data were calculated using the in-flight calibration parameters given in Allegrini et al. (2020). The electron data are computed as 1-D moments, proton data are computed from the JADE-I Species 3 plus Species 4 products, while heavy ion data come from JADE-I Species 5 (for more details see McComas et al., 2017). The heavy ion data assumes a mass/charge (m/q) ratio of 16 since O^+ and S^{++} are the dominant species. Note that the calculated density $n \propto \sqrt{m/q}$ and temperature $T \propto q$. For clarity and accuracy, we employ only those data points for which the relative uncertainty is less than 200%, though we note within this selection the errors are typically smaller than this, with, for example, median errors in the temperature of $\sim$60%, $\sim$30%, and $\sim$1% for the heavy ions, protons and electrons, respectively. The bottom panel of Figure 2 shows axial distance above the Khurana (1992) model current sheet position. Also shown in Figure 2 by the black and gray lines are model values which are discussed in section 3 below.

Considering first the poloidal field components ΔB_ρ and ΔB_z shown in Figures 2a and 2b, respectively, we note that in the middle magnetosphere these field components indicate primarily the strength of the azimuthal magnetodisc current and, to a lesser extent, the magnetopause current. The values in the southern hemisphere are, of course, actually negative, but we have plotted the magnitude of ΔB_ρ to more clearly indicate variations in the strength of the magnetodisc current, itself a signature of varying outward stress. The magnitude of ΔB_ρ exhibits a characteristic variation as the spacecraft traverses the current sheet, dropping to 0 at the center, peaking just outside and then slowly dropping with increasing distance. The values overall increase with decreasing radial distance, indicating larger magnetodisc current, though it is evident that during an interval from the end of Day 33 to the end of Day 35, ΔB_ρ was at an elevated level relative to the surrounding intervals. Specifically, at $\sim$60 R_J on Day 33, ΔB_ρ was 6–8 nT, increasing to $\sim$10–20 nT over Days 34–35 between $\sim$55 and 40 R_J, dropping thereafter to $\sim$16 nT before increasing again. This enhancement in ΔB_ρ is the manifestation of a transient increase in magnetodisc currents and associated elevated radial stress, discussed further below. The ΔB_z component was typically northward, consistent with the inner region of the current sheet, with values increasing with both decreasing radial distance and distance from the current sheet center. The larger variation in ΔB_z with latitude during the enhancement region indicates a reduction of the vertical scale height of the magnetodisc, evidently related to stretching of the disc. This is consistent with the more rapid traversals of the current sheet during the enhancement.

Turning now to the ΔB_ϕ residuals shown in Figure 2c, we note that this component also switches sign across the current sheet, with negative values in the northern hemisphere, though here we again plot the magnitude to highlight temporal variation. This component of the residual magnetic field is related to radial current and azimuthal torque. The field measured by the spacecraft follows from Ampère's law, which determines that, provided that field-perpendicular currents can be neglected in the region considered,
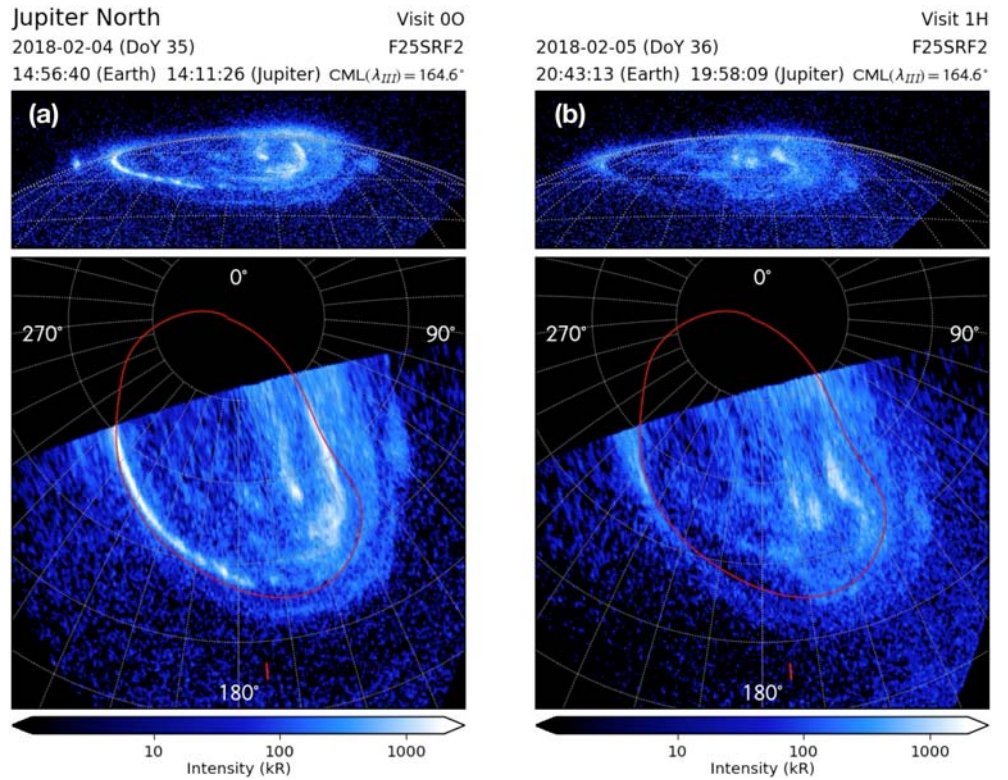
Figure 3. Figure showing HST images obtained on (a) Day 35 and (b) Day 36. Top panels show the unprojected images, while the bottom panels show projections as viewed from above with 180° System III longitude oriented toward the bottom. Images are shown on a logarithmic color map as shown with the color bar at the bottom. The Nichols et al. (2017) reference main oval is shown in red, and a 10×10 graticule is shown with gray dotted lines. The subsolar longitude is shown by the red tick mark. Target, timing, visit, filter, and CML for each image are shown at the top.

ΔB_ϕ varies along a field line as $\Delta B_\phi = \Delta B_{\phi e}(\rho_e/\rho)$, where $\Delta B_{\phi e}$ is the value just outside the current sheet at distance ρ_e, where the field penetrates the (thin) current sheet. It is evident that ΔB_ϕ also exhibits enhanced values during a similar interval to the B_ρ event. At $60\,R_J$, before the enhancement, ΔB_ϕ was ∼2–3 nT, rising to ∼7–8 nT during the enhancement interval. Inside $40\,R_J$, ΔB_ϕ dropped to ∼5–6 nT. Overall, then, these magnetic field observations indicate increased currents associated with both radial stress balance and azimuthal torque for the interval over Days 33–36.

Considering now the plasma observations shown in Figures 2d–2f, we first note that numerical moments provide a broad overview of somewhat complex plasma populations. With this in mind, we show in Figure 2d plasma temperatures which are higher for heavy ions than for the protons, which are in turn hotter than the electrons. Data have been resampled by averaging to a uniform cadence of 10 min. Numerical moments can overestimate temperatures, but it is interesting to note that all three components exhibit higher temperatures during the enhancement interval (though most noticeable in the heavy ion and electron data), being, for example, for the heavy ions ∼4–10 keV near to the current sheet in the region outside the interval and ∼9–13 keV within it. There is no strong evidence of a significant increase in the ion densities during the enhancement. Electron densities at higher latitudes are overall enhanced from ∼$2 \times 10^{-3}\,\mathrm{cm}^{-3}$ in the region beyond $55\,R_J$ to 3–9 $\times 10^{-3}\,\mathrm{cm}^{-3}$ over the first half of the enhancement interval, that is, outside ∼$48\,R_J$, before dropping to ∼$1 \times 10^{-3}\,\mathrm{cm}^{-3}$ in the second half and increasing again at the end of the enhancement inside ∼$40\,R_J$. Pressures follow a similar profile.

2.2. HST Data

We now show in Figure 3 two representative images of Jupiter's northern FUV aurora obtained by the Space Telescope Imaging Spectrograph on board HST while Juno was inbound in the middle magnetosphere

during Orbit 11. Observations were obtained as part of program GO-14634 (Grodent et al., 2018) and in this case were timed to coincide with current sheet crossings on Days 35 and 36, at radial distances of ~42 and ~30 R_J, respectively. The observations were obtained with the F25SRF2 filter, which admits H$_2$ Lyman and Werner bands, and were extracted from the raw time tag data with 30 s integration and reduced using the Boston University pipeline that has been used extensively previously (e.g., Clarke et al., 2009; Nichols et al., 2017). The images highlighted in Figure 3 were selected owing to their identical central meridian longitude, which hence avoids any variation due to different limb brightening. The times of the HST images, corrected for one-way light travel time between Jupiter and HST, are shown by the gray vertical lines in Figure 2. The Day 35 image thus coincided with the enhancement event observed in the in situ data discussed above, while the Day 36 image was obtained after the event finished. The intensities along the main emission from 180° westward around to the dawn terminator peaked in the images shown at ~3,100 kR on Day 35 and ~820 kR on Day 36. It is striking to note the elevated auroral intensities along the main emission during the enhancement event in comparison with those afterward.

3. Magnetodisc and Magnetosphere-Ionosphere Coupling Model

We have modeled the magnetodisc and magnetosphere-ionosphere coupling currents using the Nichols et al. (2015) axisymmetric magnetic vector potential model, modestly updated as discussed below and constrained by these Juno data. Details of the model can be found in Nichols (2011b) and Nichols et al. (2015), and so here we briefly describe the theoretical background and the changes from the Nichols et al. (2015) version. The model iteratively calculates the magnetic vector potential $\mathbf{A}(\rho, z) = A(\rho, z)\hat{\phi}$ from an azimuthal current distribution $\mathbf{j}_\phi(\rho, z) = j(\rho, z)\hat{\phi}$ using Ampère's law

$$\nabla^2 \mathbf{A} = -\mu_0 \mathbf{j}_\phi.\tag{1}$$

The magnetic vector potential is related to the magnetic field via $\mathbf{B} = \text{curl}\mathbf{A}$, such that the field components are given by

$$B_\rho = -\frac{\partial A}{\partial z},\tag{2a}$$

and

$$B_z = \frac{1}{\rho}\frac{\partial(\rho A)}{\partial \rho},\tag{2b}$$

and the flux function F, which is such that a field line is given by $F = $ constant, is related to the vector potential via $F = \rho A$. The azimuthal current density $\mathbf{j}_\phi$ arises from the force balance equation

$$\rho_m \frac{d\mathbf{v}}{dt} = \mathbf{j}_\phi \times \mathbf{B} - \text{div } \mathbf{P},\tag{3}$$

where ρ_m is the plasma mass density, $\mathbf{v}$ is the plasma bulk velocity, and $\mathbf{P}$ is the pressure tensor. Rearranging for the azimuthal current $\mathbf{j}_\phi$ with gyrotropic pressure gives

$$\mathbf{j}_\phi = \frac{\hat{\mathbf{b}}}{B} \times \left[\rho_m \Omega^2 \rho \, \hat{\rho} + \nabla p_\perp + (p_\parallel - p_\perp)(\hat{\mathbf{b}}.\nabla)\hat{\mathbf{b}} \right],\tag{4}$$

where ω is the plasma angular velocity and $\hat{\mathbf{b}} = (b_\rho, b_z)$ is the unit vector along the poloidal magnetic field. The three terms on the right-hand side represent the centrifugal force, pressure gradient, and pressure anisotropy forces. These terms are constrained by plasma measurements and theoretical models as described below. The model computes in each grid cell the contributions to $\mathbf{j}_\phi$ due to these force terms, and A is then calculated by summing the vector potentials associated with the axisymmetric current loops represented by each grid cell of current $\mathbf{j}_\phi$. The model is initiated using a dipole magnetic field and proceeds by iteration, with the new A_{n+1} calculated by weighted averaging with the old A_n (using weights for A_n of 1–20) in order to relax toward a converged solution. Convergence is defined to be where the average variation in A

between iterations is less than 0.1%. For the results presented below, we have employed a grid cell resolution of $0.1\,R_J$, and the outer boundary is set at $120\,R_J$, beyond the apojove of Juno.

The plasma velocity in the first term on the right-hand side is obtained in each iteration by solving the "Hill-Pontius" equation which equates the radial gradient of the plasma angular momentum per unit mass with the ionospheric torque on the equatorial plasma (Cowley et al., 2002; Hill, 1979; Nichols & Cowley, 2003, 2004; Pontius Jr, 1997), that is,

$$\frac{\rho_e}{2}\frac{d}{d\rho_e}\left(\frac{\Omega}{\Omega_J}\right) + \left(\frac{\Omega}{\Omega_J}\right) = \frac{4\pi\Sigma_P^* F_e |B_{ze}|}{\dot{M}}\left(1 - \frac{\Omega}{\Omega_J}\right), \tag{5}$$

where ρ_e is the radial distance at which the field line crosses the equatorial plane, Ω_J is the angular velocity of Jupiter equal to $1.76 \times 10^{-4}\,\mathrm{rad\,s^{-1}}$, F_e and $|B_{ze}|$ are the equatorial values of the flux function and north-south field magnitude as given by the magnetodisc model, Σ_P^* is the effective Pedersen conductance reduced from the true value Σ_P by atmospheric slippage, and $\dot{M}$ is the plasma mass outflow rate. In common with previous works, atmospheric slippage is parameterized by constant $k_s = 0.5$, such that $\Sigma_P^* = (1 - k_s)\Sigma_P$ (Huang & Hill, 1989; Millward et al., 2005).

The magnetosphere-ionosphere coupling currents are related to the plasma angular velocity via, for example, for the azimuth-integrated equatorial radial current I_ρ,

$$I_\rho = 8\pi\Sigma_P^* \Omega_J F_e \left(1 - \frac{\Omega}{\Omega_J}\right), \tag{6}$$

which is equal to twice the total ionospheric Pedersen current flowing in each ionosphere. Outside the regions of field-perpendicular current, the field-aligned current density $j_\parallel$ is such that $(j_\parallel/B)$ is constant and follows from the divergence of either the field-perpendicular ionospheric or equatorial current. For the value at the top of the ionosphere $j_{\parallel i}$ we have

$$j_{\parallel i} = \frac{B_J}{2\pi\rho_e |B_{ze}|}\frac{dI_\rho}{d\rho_e} = \frac{4B_J \Omega_J}{\rho_e |B_{ze}|}\frac{d}{d\rho_e}\left[\Sigma_P^* F_e\left(1 - \frac{\Omega}{\Omega_J}\right)\right], \tag{7}$$

where we have assumed the ionospheric field strength to be vertical and equal to twice the surface equatorial field B_J in strength. Whereas Nichols et al. (2015) employed a constant value of the Pedersen conductivity Σ_P^*, here we have updated the model to incorporate Nichols and Cowley's (2004) formulation including a Pedersen conductance $\Sigma_P^*(j_{\parallel i})$ modulated self-consistently by the auroral field-aligned current. In the former case one boundary condition is required for the solution to Equation 5, which is physically that the plasma near rigidly corotates at small radial distances. In the latter case, Equations 5 and 7 are solved simultaneously, such that a further boundary condition is required either on the plasma angular velocity or field-aligned current. Following Nichols and Cowley (2004), we define both initial conditions at a point in the outer region and iterate over one parameter to obtain the solution that nearly corotates at small radial distances. Specifically, we fix the plasma angular velocity and iterate over the field-aligned current (finally specified to 18 significant figures, the limit of x86 extended precision), and solutions are typically tracked using a backward differentiation formula to within $\sim13\,R_J$, inside which they are completed by the "first iteration" to the full solution as described by Nichols and Cowley (2004). We define the initial conditions at $90\,R_J$, well beyond the region where the auroral field-aligned current peaks, such that the field-aligned current in this region is small and essentially constant. The solution is then completed to the outer edge of the model at $120\,R_J$ using the constant conductivity given by the value of the field-aligned current at $90\,R_J$. The initial condition on the plasma angular velocity is $(\omega/\Omega_J) = 0.46$, an empirical value which provides results consistent with the Juno observations as described below and is consistent with plasma velocities in this region as observed by, for example, Kane et al. (1995). To our knowledge, no systematic survey of Juno plasma velocity observations in this region is yet published, but this should of course be examined in more detail in future works.

In our model we consider the two populations observed by Voyager and Galileo, that is, a "hot" population, traditionally taken to be the 20–40 keV "convected Maxwellian" population observed by Krimigis et al.
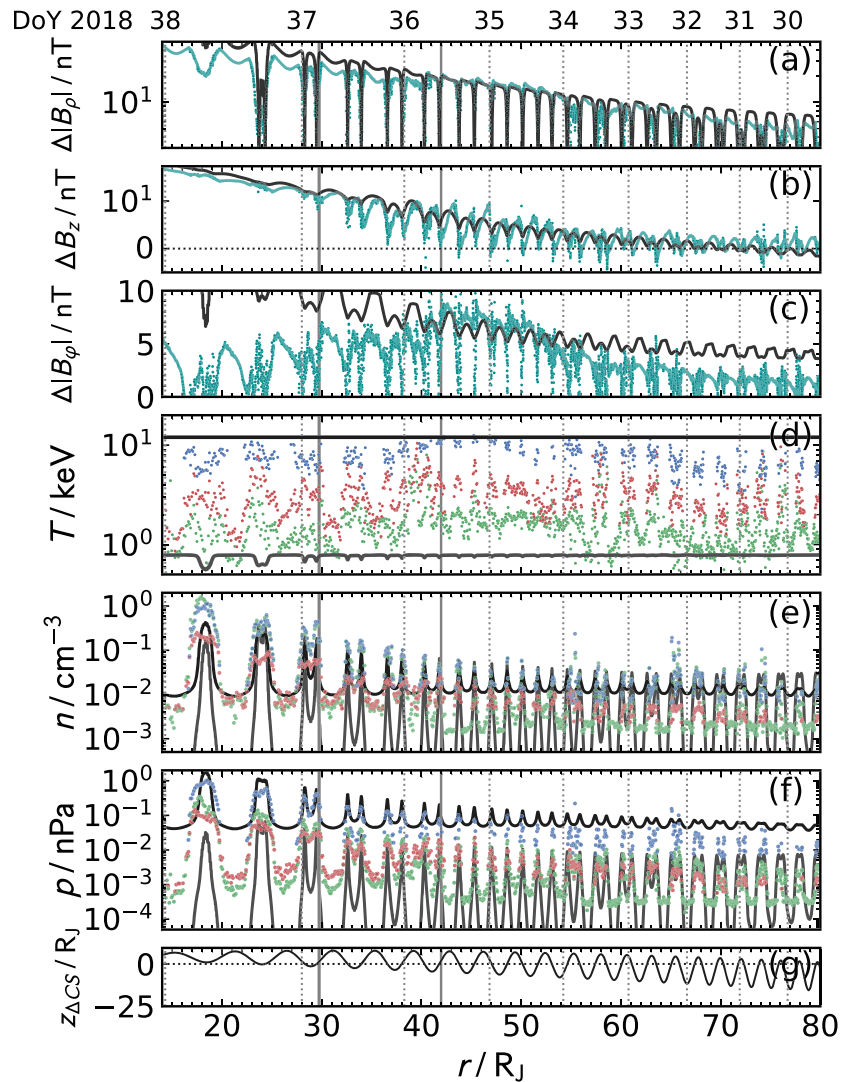
Figure 4. Plot of Juno and modeled data in the same format as for Figure 2, except that the model is for the enhancement case.

(1981) providing most of the plasma pressure and a centrifugally confined "cold" population of the order of a few hundred eV (Bagenal & Delamere, 2011; Bagenal et al., 2017; Bodisch et al., 2017; Dougherty et al., 2017; Frank et al., 2002; McNutt et al., 1981) dominating the centrifugal force. The temperatures measured by JADE shown in Figure 2d are in general between these regimes, with the electron temperatures being closer to the "cold" regime and the heavy ions being closer to the "hot" population. In this work we consider the variation in temperature discussed above to be indicative of the hot population, which dominates the plasma pressure gradient term. The hot plasma pressure is described in the model by a constant parameter $K_h = p_{h\perp} V_h$, where $p_{h\perp}$ is the hot plasma perpendicular pressure and V_h is the unit flux tube volume. From the ideal gas law for a singly ionized plasma, we also have $K_h = 2N_h k_B T_h$, where N_h is the hot plasma flux tube content, k_B is the Boltzmann constant and T_h is the hot plasma temperature, such that changes to this parameter imply variation in either temperature, density, or both. Caudal (1986) showed using Voyager and Pioneer data that $K_h = 1-5 \times 10^7$ Pa m T^{-1}, and we initially take $K_h = 2.5 \times 10^7$ Pa m T^{-1} for our model representing the nonenhancement intervals. The radial dependence of the hot plasma pressure anisotropy and the treatment of the cold population are as described in Nichols et al. (2015).

4. Modeling Results

4.1. Comparison With Juno Data

Model results appropriate to the nonenhancement intervals are shown in Figure 2. We have taken the canonical $\dot{M} = 1,000\ \mathrm{kg\,s^{-1}}$ for purposes of the solution to the Hill-Pontius equation. The poloidal field of the magnetodisc is shown by the black lines in Figures 2a and 2b. The model evidently reproduces the observed field reasonably well, particularly for the ΔB_ρ component. The broad variation of the ΔB_z component is reasonably consistent outside the enhancement region, although the amplitude of the diurnal modulation is less well modeled, being consistently less than observed. The ΔB_ϕ values outside the (assumed thin) current sheet are calculated from the total equatorial radial current given by Equation 6 using Ampère's Law, which yields

$$\Delta B_\phi = \left(\frac{\rho_e}{\rho}\right)\frac{\mu_0 I_\rho}{4\pi\rho_e}. \tag{8}$$

The drops to $\Delta B_\phi = 0$ within the equatorial current sheet, which depend on the exact nature of the gradient drifts and electrodynamics in this region, are not modeled here, and we concentrate on the values outside the current sheet. Aside from an increasing trend toward higher values in the inner region, model values are in broad agreement with the observed values outside the enhancement region.

Model plasma parameters are shown in Figures 2d–2f. As discussed above, the hot plasma is parameterized by constant K_h, such that in the model, hot plasma flux tube content and temperature are degenerate, and hence defining one parameter for a given flux tube volume sets the other parameter accordingly (note the force balance is unaffected by this choice). We thus initially define a value of 8 keV as the upper envelope of ion temperatures observed outside of the enhancement interval and is shown by the black line shown in Figure 2d. We note that this is somewhat lower than the temperatures of the hot plasma population observed by Krimigis et al. (1981) but is consistent with these data and, as discussed above, does not affect the magnetodisc solution. The model cold plasma temperatures are shown by the gray line. The plasma densities then given by the model, shown in Figure 2e, are broadly consistent with the heavy ion observations in the plasma sheet, with the centrifugally confined cold plasma peaks closely matching the observations near the plasma sheet crossings at all radial distances, and also at higher latitudes in outer region. The hot plasma values are within the scatter envelope of the ion observations at higher latitudes inside $\sim 55\ R_J$, though we note this agreement depends on the chosen temperature, as discussed above. Model plasma pressures are shown in Figure 2e, with the dominant hot plasma values shown in black and the cold plasma values shown in gray. Modeled hot plasma values tend to be higher than the observed values owing to the higher temperature, though do agree reasonably well in current sheet crossings. The modeled cold plasma pressures tend to be somewhat less than observed values, especially at larger distances from the current sheet in the inner region, with best agreement in the outer region.

It is also interesting to generate model results with parameters appropriate to the enhancement region, though we note that transient conditions may in reality differ somewhat from the results given by this steady state model. With this caveat in mind, results are shown in Figure 4. Input parameters and boundary conditions for this model run are identical to that described above, except that, to reflect the higher observed plasma temperatures and densities during this interval, the hot plasma parameter used is $K_h = 4.1 \times 10^7\ \mathrm{Pa\,m\,T^{-1}}$, and the mass outflow rate is $\dot{M} = 2,350\ \mathrm{kg\,s^{-1}}$, similar to the higher values used by Louarn et al. (2016) for periods of large azimuthal field. It is evident that the increased outward stress causes increased radial stretching of the modeled magnetodisc with, in the inner region, associated elevated ΔB_ρ and ΔB_z values along with larger variation in the latter. As noted by Cowley et al. (2002) and Nichols (2011b) the modified mapping to the ionosphere caused by the magnetodisc current changes the magnetosphere-ionosphere coupling currents. In this case, the stretched magnetodisc results in greater currents, such that the values of ΔB_ϕ are increased, consistent with the observed values in the elevated region. Considering now the plasma parameters, employing a hot plasma temperature of 12 keV appropriate for upper envelope of the heavy ion temperatures in the enhancement region as shown by the black line in Figure 4d yields plasma number densities consistent with the heavy ions in this region as shown in Figure 4e. Plasma pressures in Figure 4e are similarly consistent. However, we note that varying $\dot{M}$ without changing the cold plasma flux tube content N_c
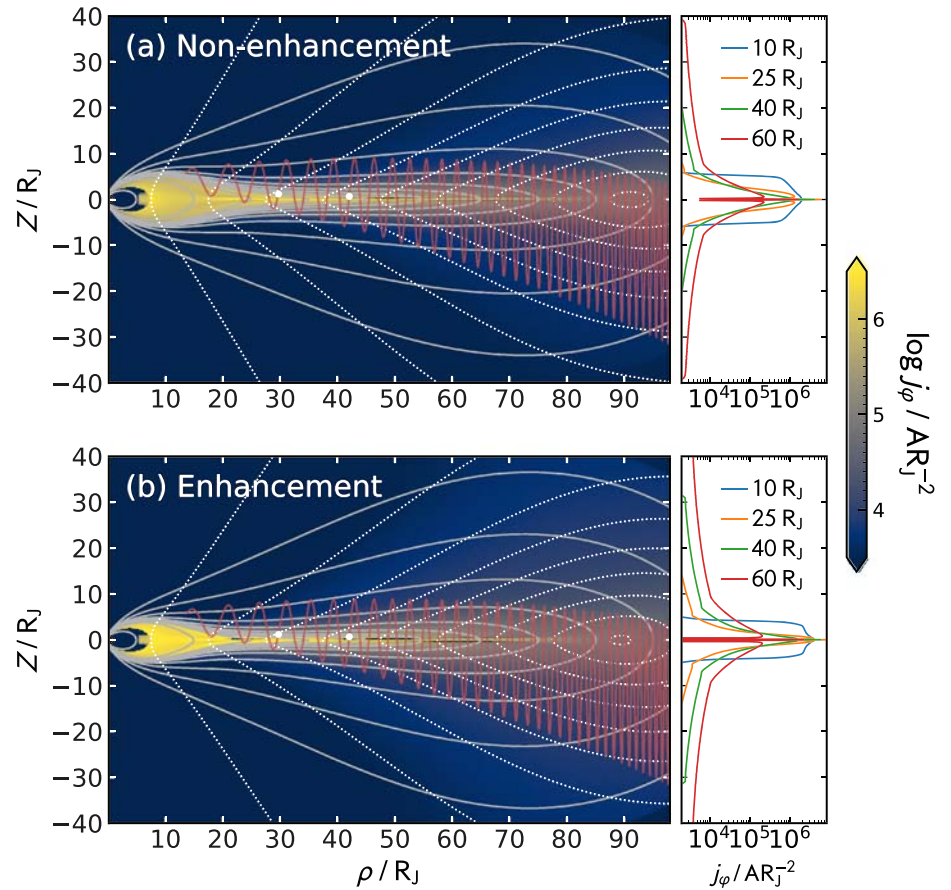
Figure 5. Plot showing modeled field lines and azimuthal current intensities for (a) the nonenhancement and (b) the enhancement cases. On the left, current sheet field lines are shown by white dotted lines, while total field lines are shown by the solid gray lines. Juno's trajectory is shown by light red lines. White points indicate Juno's location when the HST images were obtained. The colors show the logarithm of the azimuthal current densities j_ϕ in $A\,R_J^{-1}$ as indicated by the color bar to the right. The right-hand column shows vertical cuts of j_ϕ through the current sheet at the radial distances as labeled.

implies increased outward transport rate, and all variation in outward stress is then due to the pressure gradient. It is not clear whether this is always the case, though we note again that in this case there is no strong evidence of an increase in ion number densities during the enhancement. The effects on the magnetodisc of taking N_c either as a constant or a function of $\dot{M}$ were discussed by Nichols (2011b). In light of this uncertainty, we have also produced a solution appropriate for the enhancement region with $N_c \propto \dot{M}$. The results did not produce B_ϕ signatures consistent with the observations and are hence neither consistent with plasma or magnetic field observations, such that for brevity we do not show the results here. However, we note that input parameter values of $K_h = 3.8 \times 10^7\,\mathrm{Pa\,m\,T^{-1}}$ and $\dot{M} = 1,300\,\mathrm{kg\,s^{-1}}$ reproduce the enhancement poloidal field. Both parameters thus deviate somewhat less than the previous case from the nonenhancement values owing to the combined contribution to increased outward centrifugal force; however, in this case the azimuthal field is ~2 nT less than observed. We also searched for a solution for the enhancement by solely varying the initial condition on the plasma angular velocity but did not find a convergent solution that reproduced the observations.

4.2. Further Modeling Results

We now consider other model parameters important to understand the system. We first show in Figure 5 the trajectory of Juno in magnetic coordinates, along with the modeled overall and current sheet field lines. The colors indicate the total azimuthal current density j_ϕ. It is first worth noting that the current sheet exhibits
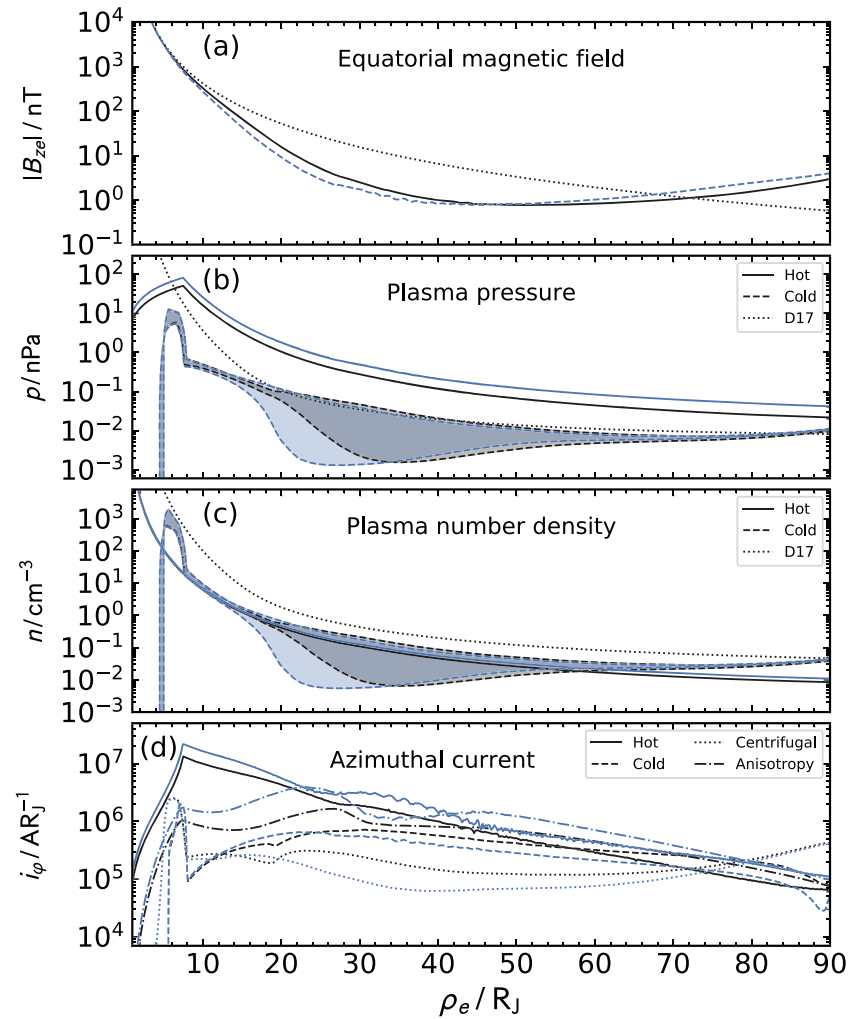
Figure 6. Plot of magnetodisc parameters for the nonenhancement (black) and enhancement (blue) cases versus radial distance ρ_e. Panel (a) shows the magnitude of the north-south field threading the equatorial plane $|B_{ze}|$ in nT. The enhancement case is shown dashed, and the dotted line shows the values for the planetary dipole alone, based on the JRM09 model (Connerney et al., 2018). Panel (b) shows the plasma pressure p in Pa. The solid lines show the equatorial perpendicular pressure $p_{\perp e}$, the filled region bounded by dashed lines indicate the range of values for the cold plasma obtained $\pm 1\,R_J$ about the equator. The dotted line shows the Dougherty et al. (2017) (D17) profile. Panel (c) shows the number density n in cm^{-3} in a similar format to panel (b). Panel (d) shows the azimuthal current intensity i_ϕ in $A\,R_J^{-1}$, vertically integrated over $\pm 3\,R_J$ about the equator. The different contributions to the current are plotted using line styles as labeled.

fine structure owing to the different contributions, with, for example, the thin (few tenths of an R_J) maximum at the equator arising principally from the anisotropy term, and the hot plasma pressure largely responsible for the overall width in the inner and middle magnetosphere. Having said that, the field signatures of such fine structure would be challenging to observe. Overall, though, the modeled current sheet is thinner when enhanced, with full widths at half maximum (FWHM) of the logarithm of the hot plasma pressure gradient current at $25\,R_J$ of ~ 2.2 and $\sim 1.2\,R_J$ in the middle magnetosphere for the nonenhancement and enhancement models, respectively.

Turning to the magnetodisc field and plasma properties, we show in Figure 6 the variation of key magnetodisc parameters with radial distance for the nonenhancement (black) and enhancement (blue dashed) models. We first show in Figure 6a the total north-south field threading the equatorial plane compared to the
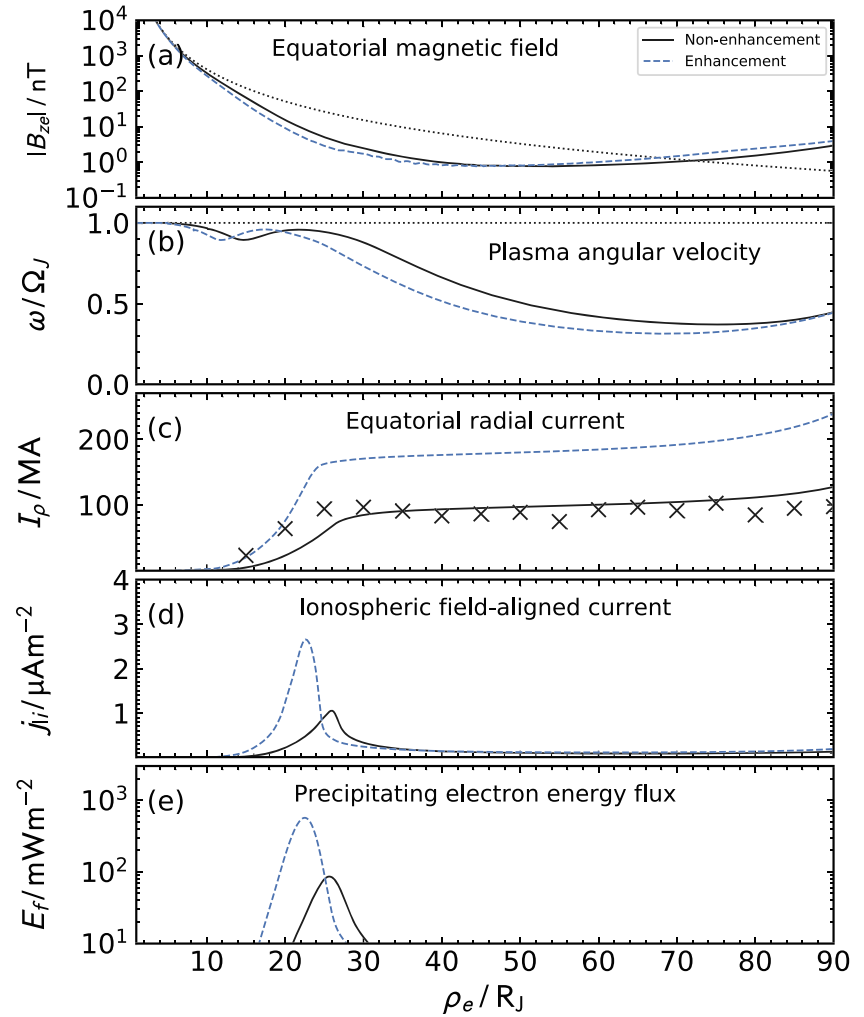
Figure 7. Plot of M-I coupling current system parameters for the nonenhancement (black solid lines) and enhancement (blue dashed lines) cases versus radial distance ρ_e. Panel (a) shows the magnitude of the north-south field threading the equatorial plane $|B_{ze}|$ in nT in the same format as for Figure 6a. Panel (b) shows the plasma angular velocity ω normalized to the planet's Ω_J. Panel (c) shows the total equatorial radial current I_ρ in MA. Also shown by the crosses are the Galileo measurements as described in the text. Panel (d) shows the ionospheric field-aligned current density $j_{\|i}$ in $\mu A\,m^{-2}$. Panel (e) shows the precipitating electron energy flux E_f in $mW\,m^{-2}$.

planetary dipole. As suggested by the residual ΔB_z profile shown in Figure 2b, for both cases the field initially drops somewhat more rapidly than for the dipole, approximately as $\rho_e^{-4.7}$ for the nonenhancement case and as $\rho_e^{-5.1}$ for the enhancement case, before flattening out at around ~1 nT in both cases. The plasma pressures and equatorial number densities are shown in Figures 6b and 6c, along with the Dougherty et al. (2017) (D17) radial profiles derived from Voyager and Galileo data. We have assumed a singly ionized plasma in the calculation of the pressure using the D17 number density and temperature profiles. The hot plasma pressure shown is the perpendicular component, which dominates the cold plasma over the whole of the region of interest, and is larger for the enhancement case with increased K_h value by factors of ~2. The centrifugally confined cold plasma pressures vary strongly with z, such that we show the range between $\pm 1\,R_J$ about the equator at a given radial distance. The enhanced case exhibits reduced off-equator plasma pressures at somewhat closer distances than for the nonenhancement case, though this difference occurs at radial distances smaller than where Juno observed the enhancement. The equatorial values exhibit excellent agreement with the D17 profile beyond ~15 R_J. The modeled number densities are somewhat lower than the D17 profiles by factors of ~2–3 over most of the magnetosphere, but this is within the

scale of the variance of the data from which the D17 profiles were derived. We further show in Figure 2d the contributions to the azimuthal current intensity i_ϕ, vertically integrated over $\pm 3\,R_J$ from the equator. For both cases the hot plasma pressure gradient current is dominant within $\sim 20\,R_J$, with the anisotropy current largest beyond $\sim 45\,R_J$, and the values for the enhanced case exceeding those for the nonenhancement case by factors of 2–3. For both cases, the cold plasma pressure term is mostly negligible in the middle magnetosphere, but for the nonenhancement case becomes comparable with the hot plasma pressure term beyond $\sim 80\,R_J$, while in both cases the centrifugal term dominates beyond $\sim 80\,R_J$.

In Figure 7 we show parameters relating to the M-I coupling current system, and we first reproduce for completeness in Figure 7a the north-south magnetic field shown in Figure 6a. The plasma angular velocities given by Equation 5 are shown in Figure 7b. They exhibit the characteristic profiles of solutions computed with self-consistent Pedersen conductance, as described by Nichols and Cowley (2004). The profiles for the two cases are largely similar and indeed converge on an identical value at $90\,R_J$ as required by the imposed boundary condition. The associated field-perpendicular current and field-aligned current densities given by Equations 6 and 7 are shown in Figures 7c and 7d. Also shown for comparison in Figure 7c are the values of the total radial current as derived by Nichols and Cowley (2004) from Galileo midnight B_z measurements given by Khurana (2001). It is evident that the radial current in the nonenhancement case is largely consistent with these values except for the location of the rise in the inner region, though this is well matched by the enhancement case, which then plateaus at values around a factor of ~ 1.8 higher. The field-aligned currents in Figure 7d peak at $\sim 1.1\,\mu\text{A m}^{-2}$ at $\sim 25\,R_J$, and $\sim 2.7\,\mu\text{A m}^{-2}$ at $\sim 22\,R_J$, respectively. Conversion from field-aligned current density to precipitating energy flux is conducted using Knight's (1973) theory, which has been shown to produce results consistent with the Juno Jupiter Energetic Particle Detector Instrument (JEDI) observations of accelerated electrons above Jupiter's auroral region (Clark et al., 2018). In this case, the precipitating energy flux is given by

$$E_f = \frac{E_{f0}}{2}\left[\left(\frac{j_{\|i}}{j_{\|i0}}\right)^2 + 1\right], \tag{9}$$

where $j_{\|i0}$ is the maximum field-aligned current that can be carried by unaccelerated precipitating magnetospheric electrons, given by

$$j_{\|i0} = eN\left(\frac{W_{th}}{2\pi m_e}\right)^{1/2}, \tag{10}$$

with a corresponding precipitating energy flux E_{f0} of

$$E_{f0} = 2NW_{th}\left(\frac{W_{th}}{2\pi m_e}\right)^{1/2}, \tag{11}$$

where e is the elementary charge, N is the magnetospheric electron number density, W_{th} is the high latitude electron thermal energy, and m_e is the electron mass. With Clark et al. (2018) we take $N = 0.018\,\text{cm}^{-3}$ and $W_{th} = 2.5\,\text{keV}$. These currents then correspond to precipitating electron energy fluxes shown in Figure 7e, peaking at ~ 86 and $\sim 560\,\text{mW m}^{-2}$ for nonenhancement and enhancement cases, respectively, values which are well within the range of those observed by Clark et al. (2018) in the accelerated distributions. Using the canonical conversion rate of $1\,\text{mW m}^{-2}$ leading to $10\,\text{kR}$ of FUV auroral intensity, these energy fluxes correspond to peak intensities of ~ 860 and $\sim 5,600\,\text{kR}$, respectively. The former is reasonably consistent with the $\sim 820\,\text{kR}$ observed peak intensity in the image taken on Day 36 shown in Figure 3b, and the latter is qualitatively consistent with increased auroral intensities on Day 35, though larger than the peak value in the image shown in Figure 3a of $\sim 3,100\,\text{kR}$ by a factor of ~ 1.8.

5. Discussion

We have presented Juno observations of Jupiter's magnetic field and plasma obtained during the inbound pass prior to PJ 11 in February 2018, along with simultaneous HST observations of the planet's auroras. We showed that a few-day transient enhancement of the azimuthal field (associated with torque acting on
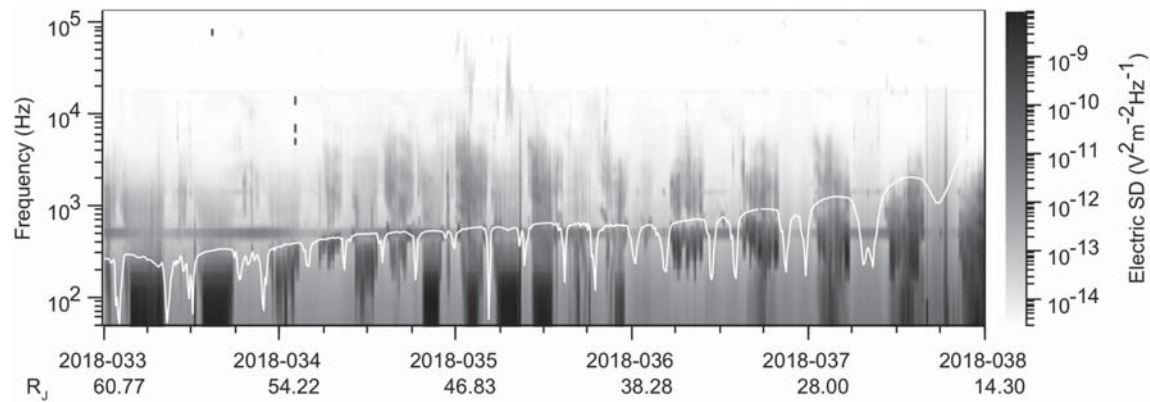
Figure 8. Plot of electric spectral density versus time as observed by the Waves instrument on board Juno.

the magnetospheric field and plasma) and radial magnetic field (associated with radial force balance) and plasma temperature was coincident with a significant brightening of Jupiter's dawn-side main emission. This represents the first evidence of control of Jupiter's main auroral emission intensity by magnetospheric current observed in situ via the magnetic field. We have reproduced Juno magnetic field and plasma observations and HST observations of Jupiter's main auroral emission intensity using a self-consistent axisymmetric model of magnetospheric force balance and magnetosphere-ionosphere coupling. We obtained solutions which broadly reproduce the field, plasma and auroral observations for the nonenhancement and the transient enhancement intervals. The modeled enhancement results were obtained by employing increased (by factors of ∼2) hot plasma temperature and iogenic plasma mass outflow rate, which are thus implicated as potential drivers of the observed effects.

It is interesting to consider the causes of the above changes. The system of equations in the model is not closed, such that the mass outflow rate is defined independently of the hot plasma temperature, though it is possible that the two are related (e.g., Abe & Nishida, 1986). Volcanic activity on Io does vary, but the time-scale of the magnetospheric response to impulsive events, for example, as observed the the intensity of UV emissions from the Io plasma torus, is months (Yoshikawa et al., 2017). It is possible that plasma outflow through diffusive "drizzle" (Kivelson & Southwood, 2005) may be enhanced during intervals when the field is particularly stretched. There was of course no in situ near-Jupiter solar wind data obtained during this interval, though as shown in Figure 8 enhanced kHz electric field spectral densities observed by the Waves instrument on Juno (Kurth et al., 2017), representing trapped continuum radiation as discussed by Gurnett (1975) and Gurnett et al. (1980), possibly indicate increased solar wind density around the enhancement interval, though the timing is somewhat uncertain. This is an interesting possibility, and is consistent with previous observations of increased ME intensity following compression region onset (Clarke et al., 2009; Nichols et al., 2009, 2017). However, there is no strong evidence of increased magnetopause currents (enhanced southward B_z in the equatorial plane), and the increased B_ρ indicates more stretched, rather than compressed, field. This may be due to the ∼3 hr local time of Juno. We then suggest the following as a plausible scenario to explain the observations. A solar wind compression may naturally yield the observed increased plasma temperatures as heated plasma convects around from the dayside. In addition, solar wind compression-induced tail reconnection of the kind observed at Saturn (Bunce et al., 2005) may release a significant quantity of mass down the tail and drive heated return flow on the dawn side. It is conceivable then that an episode of Vasyliunas cycle mass loss might enhance mass transport through the system by increasing the radial gradient in the mass content and stimulating the diffusive-type flux tube interchange process that leads to outflow. This would lead to a temporary increase in the rate of radial transport of iogenic plasma from the inner region, and thus $\dot{M}$. It is difficult to confirm such a suggestion with one spacecraft. However, it is interesting to note that in the later stage of the enhancement event, between radial distances of ∼42–48 R_J, the mean electron densities observed at high latitudes (see, e.g., Figure 2e), corresponding to flux tubes mapping to equatorial distances of ∼70–90 R_J according to the enhancement magnetodisc model, are reduced by a factor of ∼3 compared with the surrounding regions. As shown in Figures 2e and 4e, not all of this

variation, for example, the difference in the high latitude electron densities observed either side of 40 R_J, is explained by the model and is evidently a result of temporal effects. We suggest that similar studies to this of further Juno orbits will enable confirmation or otherwise of such a scenario.

In any case, our results reveal that the origin of the radio emission effects reported by Louarn et al. (2016) is indeed the main auroral emission. Our consideration in terms of the variation of a quasi steady state M-I coupling current system differs somewhat from the approach of Yao et al. (2019), who considered that changes in the field magnitudes, which they associated with loading and unloading of magnetic flux, is the salient parameter controlling the intensity of the auroral emissions, rather than the instantaneous value of B_ϕ related to the strength of the M-I coupling currents. In reality the system likely exhibits elements of both a continuous outward flow with driving of associated M-I coupling and magnetodisc currents, modulated by the rates of spontaneous and solar wind-driven mass release via reconnection in the tail.

We note that Allegrini et al. (2020) map the main auroral oval as observed by Juno UVS to 50 R_J using the JRM09 internal field model of Connerney et al. (2018) plus the Connerney et al. (1981) current sheet, whereas here we have calculated field-aligned currents mapping to 20–30 R_J. We note, however, that ionosphere-equator mappings are sensitively dependent on the azimuthal current sheet intensity, and those authors suggest that an updated current sheet model may bring the mapping inward. Further, the low altitude traversals of the main emission considered by Allegrini et al. were in the afternoon/dusk sector, whereas our magnetospheric study is in the predawn, which has a significantly different (e.g., more thin) current sheet morphology (Khurana & Schwarzl, 2005). Grodent et al. (2003) showed that the statistical main emission and the (VIP4) 20 R_J ovals can deviate by a few degrees, and the location of the main emission shifts poleward on the dusk side with increasing CML. It is also possible that the main emission in this sector may map further out if, for example, the background conductivity is higher at dusk as considered by Tao et al. (2010), who showed that conductivity effects may shift the duskside main emission poleward by ∼4° relative to dawn, accompanied by increased distance scale of the radial profile of the angular velocity with, for example, the 50% corotation radius moving from ∼15 to ∼30 R_J. Such local effects are beyond the scope of an axisymmetric model, but it would be interesting to produce results oriented toward to the dusk sector in a future study.

There are limitations to the results presented here. As noted by Caudal (1986), neither uniqueness nor stability of solutions can be demonstrated by this modeling technique. Nor have we considered local time effects, which may for example give rise to field-aligned currents associated with a partial ring current (Bunce & Cowley, 2001; Khurana, 2001) and increased noon-midnight asymmetry during compressions as modeled by Chané et al. (2017). The model is steady state, such that application to transient phenomena must be treated with a certain degree of caution. The increase in the modeled electron energy flux is higher than suggested by the HST observations by a factor of ∼1.8, which indicates either that the UV intensity response to electron energy flux is not linear or the computed electron energy flux is too high in the enhancement case. This depends on the field-aligned current density, which itself arises from rate of increase with distance of the equatorial radial current in the region inward of 25 R_J. It is unclear whether the deviation of modeled B_ϕ from the observed values in the inner region arises from an inaccurate radial dependence or temporal effects. Juno did not cross the equator at these distances during this orbit, and this will be examined in future studies using later orbits. The mass outflow rate for the enhancement is higher than the 260–1,400 kg s^{-1} range discussed by, for example, Bagenal and Delamere (2011) from plasma observations, though this is envisaged only as a temporary state, with the nonenhancement value of 1,000 kg s^{-1} lying within this range. Further developments of the model will include examining nonconstant values for K_h, and considering the protons separately to the heavy ions to more closely align with the Juno observations. We thus suggest that overall this study provides important observational and modeling evidence revealing the behavior of Jupiter's magnetosphere, while providing a platform for further development in a number of directions.

6. Summary

We have presented observations of Jupiter's magnetospheric magnetic field and plasma obtained during February 2018, along with simultaneous HST observations of the planet's auroras. We have modeled the

magnetosphere-ionosphere coupling current system and magnetodisc using an axisymmetric force balance model. Our key results are the following:

- A few-day transient enhancement of both the azimuthal field and radial magnetic field, and plasma temperature was coincident with a significant brightening of Jupiter's dawn-side main emission.
- This is the first evidence of control of Jupiter's main auroral emission intensity by magnetospheric current.
- Using the model, we obtained solutions which broadly reproduce the magnetic field, plasma, and auroral observations for both the nonenhancement and the transient enhancement intervals.
- The modeled enhancement results were obtained by employing increased hot plasma temperature and iogenic plasma mass outflow rate, which are thus implicated as possible drivers of the observed effects.
- The enhancement could have been induced by a solar wind compression, and we suggest that the increased mass outflow rate could be partly driven by solar wind compression-induced plasma loss down the tail.

Data Availability Statement

HST data are available at the MAST Archive (http://archive.stsci.edu/hst/search.php) and have the doi 10.17909/t9-69wa-4q90. The JADE data used in this study is from the JNOJ/SWJAD3CALIBRATEDV1.0 data set, Version 02 files, and obtained from the Planetary Data System (PDS) at https://pds.nasa.gov. Juno Waves data are from the JNO-E/J/SS-WAV-3-CDR-SRVFULL-V1.0 data set archived at https://pds.nasa.gov. Juno MAG data are from the JNO-J-3-MAG-CAL-V1.0 data set archived at https://pds.nasa.gov.

References

Abe, T., & Nishida, A. (1986). Anomalous outward diffusion and associated heating of iogenic ions in the Jovian magnetosphere. *Journal of Geophysical Research*, *91*, 10,003–10,011. https://doi.org/10.1029/ja091ia09p10003

Allegrini, F., Mauk, B., Clark, G., Gladstone, G. R., Hue, V., Kurth, W. S., et al. (2020). Energy flux and characteristic energy of electrons over Jupiter's main auroral emission. *Journal of Geophysical Research: Space Physics*, *125*(4). https://doi.org/10.1029/2019JA027693

Allegrini, F., Bagenal, F., Bolton, S., Connerney, J., Clark, G., Ebert, R. W., & Zink, J. L.(2017). Electron beams and loss cones in the auroral regions of Jupiter. *Geophysical Research Letters*, *44*, 7131–7139. https://doi.org/10.1002/2017GL073180

Bagenal, F., & Delamere, P. A. (2011). Flow of mass and energy in the magnetospheres of Jupiter and Saturn. *Journal of Geophysical Research*, *116*, A05209. https://doi.org/10.1029/2010JA016294

Bagenal, F., Dougherty, L. P., Bodisch, K. M., Richardson, J. D., & Belcher, J. M. (2017). Survey of Voyager plasma science ions at Jupiter: 1. Analysis method. *Journal of Geophysical Research: Space Physics*, *122*, 8241–8256. https://doi.org/10.1002/2016JA023797

Bodisch, K. M., Dougherty, L. P., & Bagenal, F. (2017). Survey of Voyager plasma science ions at Jupiter: 3. Protons and minor ions. *Journal of Geophysical Research: Space Physics*, *122*, 8277–8294. https://doi.org/10.1002/2017JA024148

Bunce, E. J., & Cowley, S. W. H. (2001). Local time asymmetry of the equatorial current sheet in Jupiter's magnetosphere. *Planetary and Space Science*, *49*, 261–274.

Bunce, E. J., Cowley, S. W. H., Wright, D. M., Coates, A. J., Dougherty, M. K., Krupp, N., & Rymer, A. M. (2005). In situ observations of a solar wind compression-induced hot plasma injection in Saturn's tail. *Geophysical Research Letters*, *32*, L20S04. https://doi.org/10.1029/2005GL022888

Caudal, G. (1986). A self-consistent model of Jupiter's magnetodisc including the effects of centrifugal force and pressure. *Journal of Geophysical Research*, *91*(A4), 4201–4221.

Chané, E., Saur, J., Keppens, R., & Poedts, S. (2017). How is the Jovian main auroral emission affected by the solar wind? *Journal of Geophysical Research: Space Physics*, *122*, 1960–1978. https://doi.org/10.1002/2016JA023318

Clark, G., Mauk, B. H., Haggerty, D., Paranicas, C., Kollmann, P., Rymer, A., & Valek, P. (2017). Energetic particle signatures of magnetic field-aligned potentials over Jupiter's polar regions. *Geophysical Research Letters*, *44*, 8703–8711. https://doi.org/10.1002/2017GL074366

Clark, G., Tao, C., Mauk, B. H., Nichols, J., Saur, J., Bunce, E. J., & Valek, P. (2018). Precipitating electron energy flux and characteristic energies in Jupiter's main auroral region as measured by Juno/JEDI. *Journal of Geophysical Research: Space Physics*, *123*, 7554–7567. https://doi.org/10.1029/2018JA025639

Clarke, J. T., Nichols, J. D., Gérard, J. C., Grodent, D., Hansen, K. C., Kurth, W. S., & Cecconi, B.(2009). Response of Jupiter's and Saturn's auroral activity to the solar wind. *Journal of Geophysical Research*, *114*, A05210. https://doi.org/10.1029/2008JA013694

Connerney, J. E. P., Acuña, M. H., & Ness, N. F. (1981). Modeling the Jovian current sheet and inner magnetosphere. *Journal of Geophysical Research*, *86*(A10), 8370–8384.

Connerney, J. E. P., Adriani, A., Allegrini, F., Bagenal, F., Bolton, S. J., Bonfond, B., et al. (2017). Jupiter's magnetosphere and aurorae observed by the Juno spacecraft during its first polar orbits. *Science*, *356*(6340), 826–832. https://doi.org/10.1126/science.aam5928

Connerney, J. E. P., Benn, M., Bjarno, J. B., Denver, T., Espley, J., Jorgensen, J. L., et al. (2017). The Juno magnetic field investigation. *Space Science Reviews*, *213*(1-4), 39–138. https://doi.org/10.1007/s11214-017-0334-z

Connerney, J. E., Kotsiaros, S., Oliversen, R. J., Espley, J. R., Joergensen, J. L., Joergensen, P. S., & Levin, S. M. (2018). A new model of Jupiter's magnetic field from Juno's first nine orbits. *Geophysical Research Letters*, *45*, 2590–2596. https://doi.org/10.1002/2018GL077312

Cowley, S. W. H., Alexeev, I. I., Belenkaya, E. S., Bunce, E. J., Cottis, C. E., Kalegaev, V. V., & Wilson, F. J. (2005). A simple axisymmetric model of magnetosphere-ionosphere coupling currents in Jupiter's polar ionosphere. *Journal of Geophysical Research*, *110*, A11209. https://doi.org/10.1029/2005JA011237

Cowley, S. W. H., & Bunce, E. J. (2001). Origin of the main auroral oval in Jupiter's coupled magnetosphere-ionosphere system. *Planetary and Space Science*, *49*, 1067–1088.

Cowley, S. W. H., Deason, A. J., & Bunce, E. J. (2008). Axi-symmetric models of auroral current systems in Jupiter's magnetosphere with predictions for the Juno mission. *Annals of Geophysicae*, *26*(12), 4051–4074.

Cowley, S. W. H., Nichols, J. D., & Andrews, D. J. (2007). Modulation of Jupiter's plasma flow, polar currents, and auroral precipitation by solar wind-induced compressions and expansions of the magnetosphere: A simple theoretical model. *Annals of Geophysicae*, *25*, 1433–1463.

Cowley, S. W. H., Nichols, J. D., & Bunce, E. J. (2002). Distributions of current and auroral precipitation in Jupiter's middle magnetosphere computed from steady-state Hill-Pontius angular velocity profiles: Solutions for current sheet and dipole magnetic field models. *Planetary and Space Science*, *50*, 717–734.

Cowley, S. W. H., Provan, G., Bunce, E. J., & Nichols, J. D. (2017). Magnetosphere-ionosphere coupling at Jupiter: Expectations for Juno Perijove 1 from a steady state axisymmetric physical model. *Geophysical Research Letters*, *44*, 4497–4505. htpps://doi.org/10.1002/2017GL073129

Dougherty, L. P., Bodisch, K. M., & Bagenal, F. (2017). Survey of Voyager plasma science ions at Jupiter: 2. Heavy ions. *Journal of Geophysical Research: Space Physics*, *122*, 8257–8276. https://doi.org/10.1002/2017JA024053

Frank, L. A., Paterson, W. R., & Khurana, K. K. (2002). Observations of thermal plasmas in Jupiter's magnetotail. *Journal of Geophysical Research*, *107*(A1), 1003. https://doi.org/10.1029/2001JA000077

Grodent, D., Bonfond, B., Yao, Z., Gérard, J. C., Radioti, A., Dumont, M., & Valek, P. (2018). Jupiter's aurora observed with HST during Juno Orbits 3 to 7. *Journal of Geophysical Research: Space Physics*, *123*, 3299–3319. https://doi.org/10.1002/2017JA025046

Grodent, D., Clarke, J. T., Kim, J., Waite Jr, J. H., & Cowley, S. W. H. (2003). Jupiter's main auroral oval observed with HST-STIS. *Journal of Geophysical Research*, *108*(A11), 1389. https://doi.org/10.1029/2003JA009921

Gurnett, D. A. (1975). The Earth as a radio source: The nonthermal continuum. *Journal of Geophysical Research*, *80*, 2751–2763. https://doi.org/10.1029/ja080i019p02751

Gurnett, D. A., Kurth, W. S., & Scarf, F. L. (1980). The structure of the Jovian magnetotail from plasma wave observations. *Geophysical Research Letters*, *7*, 53–56. https://doi.org/10.1029/GL007i001p00053

Hill, T. W. (1979). Inertial limit on corotation. *Journal of Geophysical Research*, *84*(A11), 6554–6558.

Hill, T. W. (2001). The Jovian auroral oval. *Journal of Geophysical Research*, *106*(A5), 8101–8108.

Huang, T. S., & Hill, T. W. (1989). Corotation lag of the Jovian atmosphere, ionosphere, and magnetosphere. *Journal of Geophysical Research*, *94*(A4), 3761–3765.

Kane, M., Mauk, B. H., Keath, E. P., & Krimigis, S. M. (1995). Hot ions in Jupiter's magnetodisc: A model for Voyager 2 low-energy charged particle measurements. *Journal of Geophysical Research*, *100*(A10), 19,473–19,486.

Khurana, K. K. (1992). A generalized hinged-magnetodisc model of Jupiter's nightside current sheet. *Journal of Geophysical Research*, *97*, 6269–6276. https://doi.org/10.1029/92JA00169

Khurana, K. K. (2001). Influence of solar wind on Jupiter's magnetosphere deduced from currents in the equatorial plane. *Journal of Geophysical Research*, *106*(A11), 25,999–26,016.

Khurana, K. K., & Schwarzl, H. K. (2005). Global structure of Jupiter's magnetospheric current sheet. *Journal of Geophysical Research*, *110*, 8385. https://doi.org/10.1029/2004JA010757

Kim, T. K., Ebert, R. W., Valek, P. W., Allegrini, F., McComas, D. J., Bagenal, F., & Nicolaou, G. (2019). Method to derive ion properties from Juno JADE including abundance estimates for O^+ and S^{2+}. *Journal of Geophysical Research: Space Physics*, *110*, A07227. https://doi.org/10.1029/2018JA026169

Kivelson, M. G., & Southwood, D. J. (2005). Dynamical consequences of two modes of centrifugal instability in Jupiter's outer magnetosphere. *Journal of Geophysical Research*, *110*, A12209. https://doi.org/10.1029/2005JA011176

Knight, S. (1973). Parallel electric fields. *Planetary and Space Science*, *21*(5), 741–750.

Kotsiaros, S., Connerney, J. E. P., Clark, G., Allegrini, F., Gladstone, G. R., Kurth, W. S., & Levin, S. M. (2019). Birkeland currents in Jupiter's magnetosphere observed by the polar-orbiting Juno spacecraft. *Nature Astronomy*, *3*, 904–909. https://doi.org/10.1038/s41550-019-0819-7

Krimigis, S. M., Carbary, J. F., Keath, E. P., Bostrom, C. O., Axford, W. I., Gloeckler, G., & Armstrong, T. P. (1981). Characteristics of hot plasma in the Jovian magnetosphere—Results from the Voyager spacecraft. *Journal of Geophysical Research*, *86*(A10), 8227–8257.

Kurth, W. S., Hospodarsky, G. B., Kirchner, D. L., Mokrzycki, B. T., Averkamp, T. F., Robison, W. T., Piker, C. W., et al. (2017). The Juno waves investigation. *Space Science Reviews*, *213*(1–4), 347–392. https://doi.org/10.1007/s11214-017-0396-y

Louarn, P., Kivelson, M. G., & Kurth, W. S. (2016). On the links between the radio flux and magnetodisk distortions at Jupiter. *Journal of Geophysical Research A: Space Physics*, *121*, 9651–9670. https://doi.org/10.1002/2016JA023106

Mauk, B. H., Haggerty, D. K., Paranicas, C., Clark, G., Kollmann, P., Rymer, A. M., & Valek, P. (2017). Juno observations of energetic charged particles over Jupiter's polar regions: Analysis of monodirectional and bidirectional electron beams. *Geophysical Research Letters*, *44*, 4410–4418. https://doi.org/10.1002/2016GL072286

Mauk, B. H., & Krimigis, S. M. (1987). Radial force balance within Jupiter's dayside magnetosphere. *Journal of Geophysical Research*, *92*(A9), 9931–9941.

McComas, D. J., Alexander, N., Allegrini, F., Bagenal, F., Beebe, C., Clark, G., et al. (2017). The Jovian Auroral Distributions Experiment (JADE) on the Juno mission to Jupiter. *Space Science Reviews*, *213*(1–4), 547–643. https://doi.org/10.1007/s11214-013-9990-9

McNutt, R. L. Jr., Belcher, J. W., & Bridge, H. S. (1981). Positive-ion observations in the middle magnetosphere of Jupiter. *Journal of Geophysical Research*, *86*(NA10), 8319–8342.

Millward, G., Miller, S., Stallard, T., Achilleos, N., & Aylward, A. D. (2005). On the dynamics of the Jovian ionosphere and thermosphere. IV. Ion-neutral coupling. *Icarus*, *173*, 200–211. https://doi.org/10.1016/j.icarus.2004.07.027

Nichols, J. D. (2011a). Magnetosphere-ionosphere coupling at Jupiter-like exoplanets with internal plasma sources: Implications for detectability of auroral radio emissions. *Monthly Notices of the Royal Astronomical Society*, *414*(3), 2125–2138.

Nichols, J. D. (2011b). Magnetosphere-ionosphere coupling in Jupiter's middle magnetosphere: Computations including a self-consistent current sheet magnetic field model. *Journal of Geophysical Research*, *116*, A10232. https://doi.org/10.1029/2011JA016922

Nichols, J. D., Achilleos, N., & Cowley, S. W. H. (2015). A model of force balance in Jupiter's magnetodisc including hot plasma pressure anisotropy. *Journal of Geophysical Research*, *120*, 10,185–10,206. https://doi.org/10.1002/2015JA021807

Nichols, J. D., Badman, S. V., Bagenal, F., Bolton, S. J., Bonfond, B., Bunce, E. J., & Yoshikawa, I. (2017). Response of Jupiter's auroras to conditions in the interplanetary medium as measured by the Hubble Space Telescope and Juno. *Geophysical Research Letters*, *44*, 7643–7652. https://doi.org/10.1002/2017GL073029

Nichols, J. D., Clarke, J. T., Gérard, J. C., Grodent, D., & Hansen, K. C. (2009). Variation of different components of Jupiter's auroral emission. *Journal of Geophysical Research*, *114*, A06210. https://doi.org/10.1029/2009JA014051

Nichols, J. D., & Cowley, S. W. H. (2003). Magnetosphere-ionosphere coupling currents in Jupiter's middle magnetosphere: Dependence on the effective ionospheric Pedersen conductivity and iogenic plasma mass outflow rate. *Annales Geophysicae*, *21*, 1419–1441.

Nichols, J. D., & Cowley, S. W. H. (2004). Magnetosphere-ionosphere coupling currents in Jupiter's middle magnetosphere: Effect of precipitation-induced enhancement of the ionospheric Pedersen conductivity. *Annales Geophysicae*, *22*, 1799–1827.

Nichols, J. D., & Cowley, S. W. H. (2005). Magnetosphere-ionosphere coupling currents in Jupiter's middle magnetosphere: Effect of magnetosphere-ionosphere decoupling by field-aligned auroral voltages. *Annales Geophysicae*, *23*, 799–808.

Pontius, D. H. Jr. (1997). Radial mass transport and rotational dynamics. *Journal of Geophysical Research*, *102*(A4), 7137–7150.

Ray, L. C., Achilleos, N. A., Vogt, M. F., & Yates, J. N. (2014). Local time variations in Jupiter's magnetosphere-ionosphere coupling system. *Journal of Geophysical Research: Space Physics*, *119*, 4740–4751. https://doi.org/10.1002/2014JA019941

Ray, L. C., Ergun, R. E., Delamere, P. A., & Bagenal, F. (2010). Magnetosphere-ionosphere coupling at Jupiter: Effect of field-aligned potentials on angular momentum transport. *Journal of Geophysical Research*, *115*, A09211. https://doi.org/10.1029/2010JA015423

Smith, C., & Aylward, A. D. (2009). Coupled rotational dynamics of Jupiter's thermosphere and magnetosphere. *Annales Geophysicae*, *27*(1), 199–230.

Smith, E. J., Davis, L. Jr., Jones, D. E., Coleman, P. J. Jr., Colburn, D. S., Dyal, P., & Frandsen, A. M. A. (1974). The planetary magnetic field and magnetosphere of Jupiter: Pioneer 10. *Journal of Geophysical Research*, *79*(25), 3501–3513.

Southwood, D. J., & Kivelson, M. G. (2001). A new perspective concerning the influence of the solar wind on the Jovian magnetosphere. *Journal of Geophysical Research*, *106*(A4), 6123–6130.

Szalay, J. R., Allegrini, F., Bagenal, F., Bolton, S., Clark, G., Connerney, J. E., & Wilson, R. J.(2017). Plasma measurements in the Jovian polar region with Juno/JADE. *Geophysical Research Letters*, *44*, 7122–7130. https://doi.org/10.1002/2017GL072837

Tao, C., Fujiwara, H., & Kasaba, Y. (2009). Neutral wind control of the Jovian magnetosphere-ionosphere current system. *Journal of Geophysical Research*, *114*, A08307. https://doi.org/10.1029/2008JA013966

Tao, C., Fujiwara, H., & Kasaba, Y. (2010). Jovian magnetosphere–ionosphere current system characterized by diurnal variation of ionospheric conductance. *Planetary and Space Science*, *58*(3), 351–364.

Vasyliunas, V. M. (1983). Plasma distribution and flow, *Physics of the Jovian magnetosphere* (pp. 395–453). Cambridge, UK: Cambridge University Press.

Yao, Z. H., Grodent, D., Kurth, W. S., Clark, G., Mauk, B. H., Kimura, T., & Levin, S. M. (2019). On the relation between Jovian aurorae and the loading/unloading of the magnetic flux: Simultaneous measurements from Juno, Hubble Space Telescope, and Hisaki. *Geophysical Research Letters*, *46*, 11,632–11,641. https://doi.org/10.1029/2019GL084201

Yoshikawa, I., Suzuki, F., Hikida, R., Yoshioka, K., Murakami, G., Tsuchiya, F., & Fujimoto, M. (2017). Volcanic activity on Io and its influence on the dynamics of the Jovian magnetosphere observed by EXCEED/Hisaki in 2015. *Earth, Planets and Space*, *69*(1), 110. https://doi.org/10.1186/s40623-017-0700-9